ELSEVIER

Electronic energy dynamics of photoexcited ternary Zintl phase LiSbTe₂ and the distance estimation between trap sites

Seung-Gu Kang [a], Weon-Sik Chae [a], Yong-Rok Kim [a,*], Jin-Seung Jung [b], Sung-Han Lee [c]

[a] *Department of Chemistry, Yonsei University, Shinchon-Dong 134, Seodaemun-Gu, Seoul 120-749, South Korea*
[b] *Department of Chemistry, Kangnung Nat'l University, Kangnung 210-702, South Korea*
[c] *Department of Chemistry, Yonsei University, Wonju 220-701, South Korea*

Received 31 January 2000

Abstract

For newly synthesized ternary Zintl phase LiSbTe₂, absorption, fluorescence, and excitation spectra indicate that it has an E_g of 4.46 eV, and there is an absorption band around 300 nm below the band gap and a Stokes-shifted fluorescence band around 390 nm. At both room temperature and 77 K, power dependent steady-state and time-resolved fluorescence studies result in the appearance of another fluorescence band at about 450 and 520 nm. As the photon power increases, the 390 nm band is blue shifted at the saturation stage with the saturation of the 520 nm band as well. Along with fluorescence lifetime data, the results imply that the 390 and 450 nm bands correspond to shallow trapped exciton state and deep self-trapped exciton state originating from lattice distortion, respectively, and the 520 nm band is from the surface trap state coupled to the frozen solvent environment. The upper limit distance between the trap sites corresponding to 390 nm band is estimated to be about 17.6 nm by the dielectric function calculation of the gas phase model. © 2000 Elsevier Science B.V. All rights reserved.

Keywords: Electronic energy dynamics; Zintl phase; LiSbTe₂; Trapped exciton; Lattice distortion; Power dependent study; Fluorescense lifetime; Dielectric function

1. Introduction

A great deal of effort has been devoted to the preparation and the characterization of Zintl phase materials, which consist of alkali or alkaline earth metals and transition metals as cations and main group elements as anion units. The coexistence of ionic and covalent bonds in intermetallic phases was investigated by Eduard Zintl for the first time. The name of Zintl phase follows Zintl's contributions to this field. For NaTl, Tl atoms form a diamond network structure in which anion charges are compensated by donation of valence electrons from Na, which is located near the Tl atoms. As a result of electron transfer from cation to counter anion, most Zintl phases exhibit the characteristics of a normal valence anion unit, which retains 8-N rule of classical valence rule for insulators. However, they show metallic lustre and brittle properties in contrast to insulators and typical intermetallic phases. To explain such

---

* Corresponding author. Tel.: +82-2-361-2646; fax: +82-2-364-7050.

E-mail address: yrkim@alchemy.yonsei.ac.kr (Y.-R. Kim).

properties, Klemm proposed the pseudoatom concept for the anion unit, which would show structural characteristics of complicated multiple and cluster bondings as well as the possibility of vacancy formation. Most Zintl phase materials exhibit a variety of structural morphologies satisfying the Zintl–Klemm concept, which is the combination of Zintl's proposition and Klemm's pseudoatom concept. Since Zintl phase materials lie at the so-called ''Zintl border'', they are often considered to be semiconductors between insulators and intermetallic phases [1,2].

For the last several decades, binary and ternary Zintl phase materials containing chalcogenides (i.e., S, Se, or Te) have been extensively studied for their structural, electronic, magnetic, and optical properties [3–9]. In particular, the tellurides exhibit a wide range of novel properties in solutions and solid salts due to their various structural possibilities in which each atom is more than two coordinated [9]. Haushalter et al. reported ternary tellurides of the type M_2SnTe_4 (M = Cr, Mn, Fe, Co), which show spin-glass property in amorphous forms [10–12]. Jung et al. prepared intermetallic compounds of the formula $M_3(SbTe_3)_2$ (M = Cr, Mn, Fe, Co, Ni) by rapid precipitation of metal halides and the Zintl phase of K_3SbTe_3 as a precursor in polar solvent [1]. $M_3(SbTe_3)_2$ ternary intermetallic compounds show spin-glass behavior at the extremely low temperature of 3–5 K at which magnetic bubble [13] or magnetic hole [14] is generated under irradiation of laser. The unusual magnetic domain generation is caused by local disruption of the spin-glass state in amorphous morphology [15]. The potential applications of Zintl phase materials and intermetallic compounds to semiconductor and bubble memory devices require more fundamental spectroscopic information on band gap, electronic energy state, and electronic response time, etc.

Recently, Zintl phase $LiSbTe_2$ was newly synthesized from a solid state reaction process at the temperature of 941 K and the detailed synthetic procedure was reported in Ref. [16]. Kovba et al. reported X-ray powder diagram that was indexed as a cubic NaCl type structure with the lattice parameter of $a = 610.906(7)$ pm [17]. From the crystal structure, It is known that Li and Sb atoms are randomly occupied in Na position. Evain et al. reported that the anharmonicity structural analysis indicated a strong atomic displacement of lattice atoms due to the size difference between Li and Sb. The maximum electron density of cation site was, therefore, found quite different from that of the octahedral center due to the high polarizing property of Li [16]. Moreover, net covalent bonding character in $LiSbTe_2$ due to the unique property of Li atom makes it different from conventional Zintl phase materials.

In this study, we report the electronic energy states of Zintl phase $LiSbTe_2$ and their electronic energy dynamics for the first time. For these studies, steady-state absorption and fluorescence studies, excitation power dependent steady-state fluorescence and time-resolved fluorescence studies at both room and liquid nitrogen temperatures were employed.

In addition to the electronic energy dynamic studies, the trial method to estimate the distance between the trapped exciton sites is suggested by the measurement of the optical absorption spectra and the calculations using the gas phase model for the excitons in solid lattice, based on the blue shift phenomenon of a specific emission band at the band saturation which depends on photon power density.

2. Experimental detail

2.1. Sampling

Zintl phase, $LiSbTe_2$, of a metallic gray crystalline was finely ground and the fine powder type specimen with 100 nm average diameter of SEM image was used in the experiment. It is air stable and insoluble in polar solvents due to its covalent bonding characteristic of $Li^0Sb^0(Te^0)_2$ rather than the ionic bonding of $Li^+Sb^{3+}(Te^{2-})_2$ or $Li^+Sb^+(Te^-)_2$ [16].

At room temperature, highly viscous ethylene glycol was used as a supporting medium for the powder type sample. For low temperature (77 K) measurement, transparently frozen ethanol and a

quartz NMR tube and an optical Dewar bottle were utilized.

2.2. Steady-state absorption and fluorescence

The absorption and fluorescence spectra were measured with a UV–VIS spectrophotometer (Shimadzu, UV-160A) and a fluorimeter (Hitachi F-4500), respectively. In addition to the absorption and emission spectra, the fluorescence excitation spectra were also measured.

The optical pathlength was estimated from the average particle size of 100 nm, the density (11.42 g/cm^3), and the amount per unit area, which was used to obtain the absorption coefficient and also for the calculation of the distance between the trap sites.

2.3. Photon power dependent steady-state and time-resolved fluorescence

For the power dependent studies, the fundamental wavelength of 337 nm from a pulsed N$_2$ laser (Laser Photonics LN1000) was used for high power photon source, which has about 800 ps pulse duration and the maximum energy of 1.4 mJ per pulse. The various excitation power was controlled by using the combination of calibrated neutral density filters.

A photomultiplier tube (Hamamatzu R-928) and a monochromator (Acton Research Corp. SpectraPro-275) were connected to a *xy*-plotter for steady-state measurements and a 500 MHz digital oscilloscope (Hewlett Packard 54520A) was applied for time-resolved fluorescence at various photon powers. To remove the Rayleigh and Raman scattering, the high frequency cutoff filter was placed before the detection setup.

Finally, in order to obtain the lifetimes and the corresponding amplitudes, the time-resolved fluorescence signals were fitted through iterative least square exponential deconvolution process with an instrumental response function (IRF) measured at the same condition. Although the quality of the time-resolved fluorescence signals do not appear as good due to electrical noise, they were well fitted with IRF as shown in Fig. 4(a).

3. Results and discussion

3.1. Electronic energy states of Zintl phase LiSbTe$_2$

The absorption spectrum of Zintl phase LiSbTe$_2$ is shown in Fig. 1. Generally, the band gap energy of a solid state semiconductor can be estimated from the red edge of its absorption. The spectral shape of the band gap transition does not exhibit the Lorentzian or Gaussian structure but a continuously growing shape from the start of the band gap transition. The direct band gap energy of Zintl phase LiSbTe$_2$ can be estimated from the absorption spectra of Fig. 1 as about 278 nm (4.46 eV), which is fitted by the equation: $\alpha(\omega)hv = A(hv - E_g)^{1/2}$, where $\alpha(\omega)$ is the absorption coefficient, hv is the photon energy, and E_g is the direct band gap. Fig. 1 indicates an absorption shoulder at about 300 nm which is responsible for the confined electronic absorption state corresponding to the fluorescence band, as shown in the inset of Fig. 1. Therefore, it is considered that the absorption band around 300 nm is not from a phonon-involved indirect absorption process but a weakly bounded electron–hole paired exciton
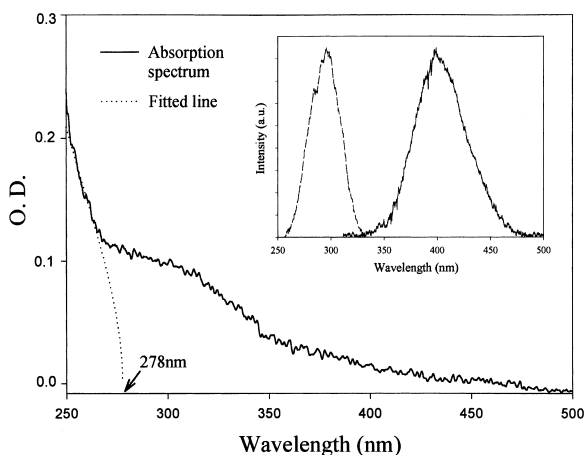

Fig. 1. Absorption spectrum of Zintl phase LiSbTe$_2$ at room temperature. The inset is the steady-state excitation spectrum $(\cdots)$ at the 400 nm detection and the fluorescence spectrum (—) at the 300 nm excitation at 77 K. The arrow mark indicates the direct band gap estimated from the parabolic fitting of the absorption spectrum.

state, which often presents lower than the frequency of the band gap transition [18].

The inset of Fig. 1 shows the fluorescence spectrum excited at 300 nm and the fluorescence excitation spectrum detected at 400 nm at 77 K. Both the excitation and fluorescence spectra have a mirror image with a large Stokes shift of about 100 nm. In the liquid phase, the intrinsic Stokes shifted fluorescence can occur due to the different degree of stabilization during solvation process in its excited and ground states. However, in the solid phase, the large Stokes shift can occur by the self-trapping of exciton or biexciton in a solid lattice at its excited state and matrix stabilization [19].

3.2. Electronic energy dynamics of Zintl phase LiSbTe₂

The steady-state absorption and emission studies indicate that the Zintl phase $LiSbTe_2$ has a band gap energy of about 4.46 eV and at least one sub-band gap of the electronic energy state, which induces a large Stokes shifted fluorescence. Fig. 2(a) and (b) shows the power dependent steady-state fluorescence spectra at room temperature and 77 K, respectively.

The fluorescence intensity increases at room temperature, with the peak at about 390 nm and shoulders at about 450 and 520 nm as the excitation power density increases. The peak at 390 nm was also observed in the low power steady-state fluorescence of the inset of Fig. 1. However, the shoulders at 450 and 520 nm did not obviously appear in the low power result. These shoulders become more clearly observed in the power dependent steady-state fluorescence spectra at 77 K and, as shown in Fig. 2(b), the 450 nm fluorescence band is even more intense than the 390 nm band contrary to the result of the room temperature case. As the excitation power increases at 77 K, 450 nm band consistently increases whereas the 390 nm band becomes saturated at the excitation power density of 4.77×10^7 mW/mm². To observe the changes of the peak position and area of each band more precisely, the fluorescence spectra at 77 K were fitted with the Gaussian functions. The fitted sub-bands of the spectrum at the excitation power density of 7.54×10^7 mW/mm² is shown in
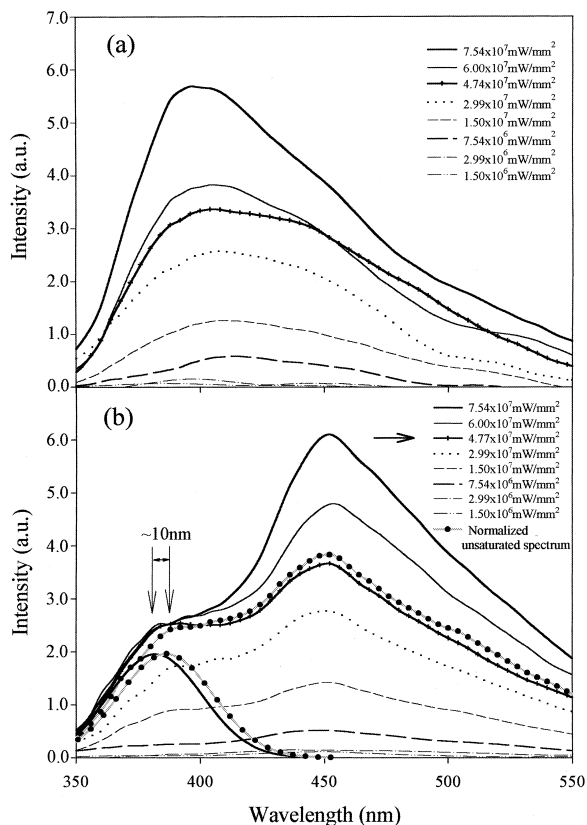

Fig. 2. (a) Steady-state fluorescence spectra of Zintl phase LiSbTe₂ at room temperature with various laser power densities. (b) Steady-state fluorescence spectra of Zintl phase LiSbTe₂ at 77 K with various laser power densities. It is shown that the 390 nm band of the saturated fluorescence spectrum becomes blue shifted by 10 nm, compared to the unsaturated spectra. The laser power density of the saturation point is marked with the arrow (→).

Fig. 3(a). It seems that the fluorescence spectra consist of at least three Gaussian sub-bands, which are peaked at 380, 450, and 520 nm at this saturation power.

From the band fitting results, the two interesting points are recognized. The first is the saturation of the 390 and 520 nm bands. The second is the blue shift of 390 nm band with its band saturation. Fig. 3(b) represents the relative integrated areas of three fitted Gaussian bands. It is observed that the 520 nm band saturates at the lowest excitation power of 2.99×10^7 mW/mm², and the
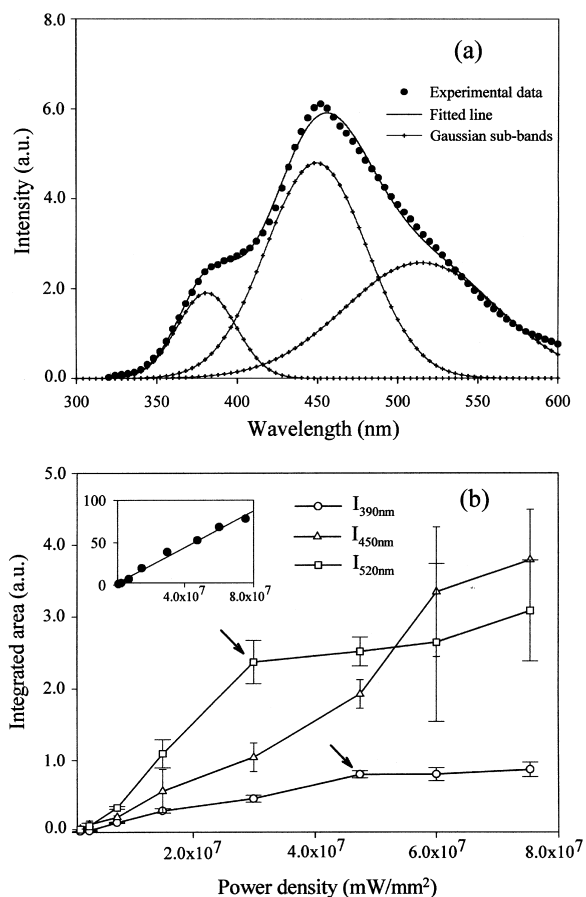
Fig. 3. (a) Steady-state fluorescence spectrum at the excitation power density of 7.54×10^7 mW/mm^2 fitted with three Gaussians. (b) Integrated areas (I) of each fluorescence band according to various laser power densities: the inset shows the linear dependence of $I_{total}(= I_{390 \ nm} + I_{450 \ nm} + I_{500 \ nm})$ to the excitation power density. The arrow marks indicate the saturation points.

390 nm band becomes saturated at 4.77×10^7 mW/mm^2. On the other hand, the intensity of the 450 nm band increases more rapidly as the 390 and 520 nm bands begin to saturate. The inset in Fig. 3(b) indicates the linear dependence of total fluorescence intensities to the excitation power, implying the exclusion of any nonlinear process. From this respect, it is known that, at the low excitation power, the intensity of each band increases without band saturation, however, as the excitation power increases, the 390 and 520 nm

bands become saturated and the excited state populations of these bands are transferred to the 450 nm band. These saturation phenomena are also shown in the results of time-resolved fluorescence measurements. At room temperature, there are not any noticeable changes of the 400 and 450 nm fluorescence decay curves with the change of the excitation power. On the other hand, the amplitudes of the time-resolved fluorescence lifetimes were changed depending on the excitation power at 77 K. Fig. 4(b) and (c) shows the fitted lifetimes at 400 and 450 nm detection wavelengths, respectively, and Fig. 4(a) represents a typical deconvoluted exponential fitting.

The fluorescence decay at 400 nm detection shows two exponential decay components, which are 3 and 14 ns and the 450 nm fluorescence emission indicates 4 and 14 ns lifetimes. In Fig. 3(a), it is shown that there are two sub-bands of 380 and 450 nm at 400 nm emission, and the 450 and 520 nm bands contribute to the 450 nm detection. In each case, after the saturation points, the relative amplitude of the slow component increases and that of the fast component decreases with increasing excitation power. It also supports the fact that the populations of the 380 and 520 nm emission states are transferred to the 450 nm emission state after their saturations. From all the points above, we can assign that the lifetimes of 3, 14, and 4 ns correspond to the 380, 450, and 520 nm emission states, respectively.

There are two possible explanations for the nonlinear increase of the 450 nm emission and the saturation of 380 and 520 nm states as follows. One is a high-density excitation effect in which recombinations caused by collisions, such as electron–hole, electron–exciton, and exciton–exciton collisions, increase as the number of the photoexcited carriers increase [20]. The other is the change of the photoexcited carrier recombination route because of the population saturation. When LiSbTe$_2$ is excited below the saturation power, some of the photoexcited species relax through radiative recombination paths without the saturation of the fluorescence state, and the others relax into the lower energy trapped states with fast nonradiative decays. The increase of the excitation power induces the saturation of
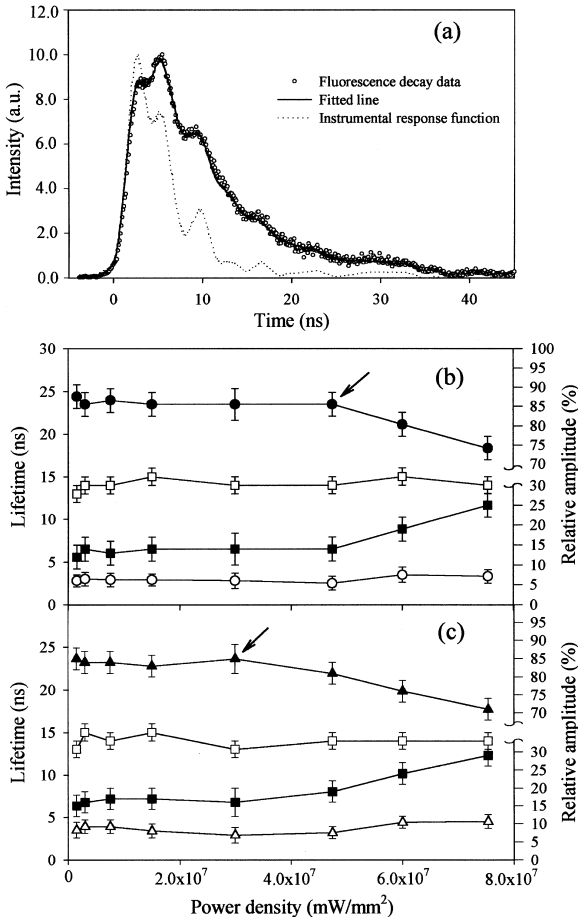
Fig. 4. (a) Typical deconvolution fitting of the time-resolved fluorescence decay signal. (b) Fitted parameters of the fluorescence decay of Zintl phase LiSbTe$_2$ at 400 nm detection with various laser power density (77 K); (○) fast lifetime component (~3 ns), (●) normalized amplitude of fast component, (□) slow lifetime component (~14 ns), (■) normalized amplitude of slow component. (c) Fitted parameters of the fluorescence decay at 450 nm detection (77 K); (△) fast lifetime component (~4 ns), (▲) normalized amplitude of fast component, (□) slow lifetime component (~14 ns), (■) normalized amplitude of slow component. The arrow marks indicate the saturation points.

radiative recombination centers and then the fluorescence intensities from the recombination sites do not increase any more with the excitation power. It is the point where the excess population of the upper 390 nm saturated states begins to be transferred into the unsaturated 450 nm emission state at the photon density of 4.77×10^7 mW/mm^2

and also the saturated lower state of the 520 nm band also starts to transfer to the 450 nm state at the photon density of 2.99×10^7 mW/mm^2; therefore, its excess population being transferred at the 450 nm emission state results in the fluorescence intensity increasing more rapidly [21,22]. Although either of these two mechanisms can be expected to occur with increasing excitation power, the result of the fluorescence lifetime indicating no dependence of photon density supports the population saturation model. Generally, as mentioned in the Section 3.3, when the recombination is caused by the collision mechanism, the lifetimes should become faster as excitation photon density increases.

The other noticeable point is the blue shift of the 390 nm band. From the three bands, convolution fitting of the power dependent steady-state fluorescence spectra at 77 K, the blue shift of approximately 10 nm was observed at the 390 nm band, whereas there is no distinguishable band shift for the other bands within our experimental error range. Fluorescence spectra were compared, in Fig. 2(b), before and after the band saturation. The blue shift of 390 nm band occurs with the population saturation. Such a shift has been known, in ZnS, from the following relationship between the band gap energy E_g and the fluorescence energy E_{trap} at the electronic energy trap state [23]:

$$E_{trap} = E_g - (D_+ + D_-) + \frac{e^2}{4\pi\varepsilon R}, \qquad (1)$$

where E_{trap} is the fluorescence energy of the electronic energy trap state, E_g is the band gap energy, $D_+ D_-$ is the trap depth, and R is the distance between the two trapped charges. When the sample is excited by low excitation power, there is no blue shift observable since the distance, R, between the trapped charges contributing to the radiative recombination is far enough to be ignored for the last term in Eq. (1). However, when the distance between the two trapped charges becomes close enough to interact each other with the population saturation, the last term of Eq. (1) cannot be negligible. This effect causes the blue shift of the saturated fluorescence band.

3.3. Characteristics of each electronic energy state in Zintl phase LiSbTe₂

The laser fluence dependence of the relaxation process can be explained as follows. The simple model to this process is given by the following kinetic equation [24]:

$$\frac{\partial[S]}{\partial t} = \alpha_S - \beta_S[S] - \gamma_S[S]^2, \tag{2}$$

where [S] represents the concentration of singlet exciton, α_S is the singlet exciton generation rate constant, β_S is the direct mono excitonic recombination rate constant, and γ_S is the direct recombination rate constant by exciton collision. At a low concentration of singlet excitons, $\beta_S[S] \gg \gamma_S[S]^2$. Thus, Eq. (2) is reduced to $\partial[S]/\partial t = \alpha_S - \beta_S[S]$. It implies that, at low exciton concentration, the singlet exciton–singlet exciton interaction is negligible, and therefore, the major relaxation route is expected to be through mono-excitonic decay channel [25]. For high concentration of singlet excitons, $\beta_S[S] \ll \gamma_S[S]^2$. Then Eq. (2) is reduced to $\partial[S]/\partial t = \alpha_S - \gamma_S[S]^2$. In this case, the typical singlet exciton annihilation process involves the following exciton–exciton collision processes [25]:

$$S_1 + S_1 \rightarrow S_1^* + S_0 \rightarrow S_1 + S_0 + phonon \tag{3}$$

$$S_1 + S_1 \rightarrow e + h \tag{4}$$
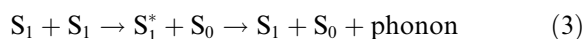
where the asterisk (*) denotes a state of high vibrational excitation (hot excitons). Typically, it undergoes a fast relaxation process in which S_1^* is nonradiatively deactivated to the S_1 state.

Under the extremely high laser fluence condition and the case of inelastic collisional process, since the multiple particle interactions can occur in the diverse ways, such as, singlet exciton–singlet exciton, singlet exciton–triplet exciton, and singlet exciton–charge carrier collision, much faster relaxation than the monoexcitonic decay are usually observed [25]. In our time-resolved fluorescence results, however, for the range of the applied excitation power density, any change of the lifetime components was not observed. Therefore the not-so-prevalent exciton–exciton collision channel does not account for the observed laser fluence

dependence of the photoexcited decay behavior in this study.

The temperature dependence of the time-resolved fluorescence decay curves at both room and liquid nitrogen temperatures was investigated at the low excitation power without the saturation. Fig. 5(a) and (b) shows the comparison of the room and low temperature fluorescence decays detected at 400 and 450 nm, respectively. Fig. 5(a) shows that the time-resolved fluorescence at 77 K decays faster than that at room temperature. It implies that, at the 400 nm detection, the amplitude of the fast component becomes greater at liquid nitrogen temperature. On the other hand, Fig. 5(b) indicates that the fluorescence decay curves of the 450 nm emission show less
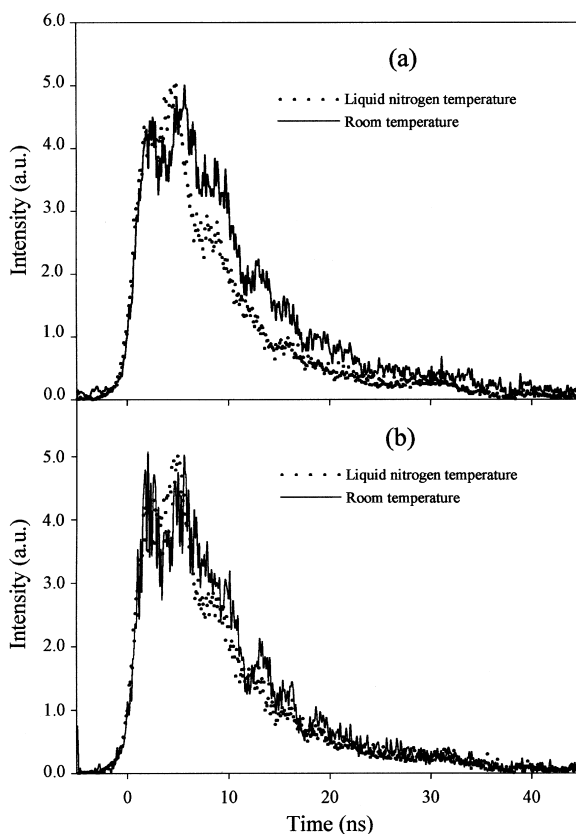

Fig. 5. (a) Time-resolved fluorescence decay curves of Zintl phase LiSbTe₂ detected at 400 nm and 1.50×10^6 mW/mm² at room temperature and 77 K. (b) Time-resolved fluorescence decay curves of Zintl phase LiSbTe₂ detected at 450 nm and 1.50×10^6 mW/mm² at room temperature and 77 K.

temperature dependence. If the dominant mechanism limiting the mean free path in exciton diffusion is the scattering by phonons, the diffusion coefficient of exciton $D(T)$ should be proportional to $T^{-1/2}$ [26]. According to this model, phonon modes decrease, as the temperature is lowered, so that exciton can diffuse longer distance in solid lattice with less interference between phonons and excitons. Therefore, the number of exciton collision, which causes radiative recombination in lattice becomes greater and results in relatively larger amplitude of the fast component. At a higher temperature, however, lots of phonon modes existing in the solid lattice interfere with the exciton diffusion through the lattice so that the number of exciton collisions for radiative recombination becomes smaller [26]. The fast component, therefore, has a relatively small amplitude. Such temperature dependence of the lifetime implies that the 390 nm fluorescence band which has the fast component of 3 ns may occur from the free exciton or the shallow trapped exciton states. Furthermore, the temperature dependence of the 390 nm band at the low temperature and the saturation phenomenon at high laser fluence strongly suggest that the 390 nm band is from the phonon coupled shallow trapped exciton state with diffusive recombination governed by the processes such as exciton–phonon scattering.

As shown in Fig. 5(b), little temperature dependence of 450 nm band suggests that it is due to deep trapped localized exciton states. In fact, the lattice local disorders of Zintl phase $LiSbTe_2$ from the lattice distortion cause the formation of localized exciton states [16] and bring the enhancement of self-trapping processes to these states [19]. The possible factors for the lattice distortion may come from the atomic size difference between Li and Sb, which are randomly positioned at the cationic site of NaCl type octahedral sites of $LiSbTe_2$ and the higher polarizing property of Li compared to Sb, which makes the electron density maximum of Li cation different from the normal cationic octahedral center [16].

The characteristics of 520 nm band are still uncertain. However, it is thought that the major decay channel of this state occurs probably from the surface trap states by the interactions between the surface state of $LiSbTe_2$ and the frozen glassy ethanol solvent environment. Chestnoy et al. suggested that the excited electrons were quickly trapped into impurity sites or defect centers, which can either transfer the electron to a surface molecular acceptor or recombine with the nearest pre-existing trapped hole [27]. The spectral broadening of 520 nm emission may come from the inhomogeneity of the size distribution of the sample. In addition, at room temperature, the contribution of this band to the total fluorescence is small, and it is not saturated at high laser fluence, which is probably due to the large thermal interaction with the solvent environment. At the low temperature of 77 K, however, the less thermal interaction with solvent enhances the contribution of this emission and it becomes saturated under high laser fluence and furthermore, the excess population of this state is transferred to 450 nm self-trapped localized states, probably, through the significant spectral overlap between 450 and 520 nm fluorescence bands.

3.4. The calculation of the upper limit distance between two shallow trapped excitons

As previously mentioned in Section 3.2, it was observed that there was an approximately 10 nm blue shift of the 390 nm band at the saturation excitation power. The blue shift of this band can be interpreted by the increase of the third term in Eq. (1), which is caused by the shortened distance between the shallow trapped excitons. Now, it is suggested that the distance, R, between the shallow trapped excitons at the beginning of the saturation point can be estimated using Eq. (1) and the permittivity (ε) in this media by treating excitons in lattice as the gas phase harmonic oscillator [28].

The fluorescence energy of the trapped state E_{trap} is explained by Eq. (1) as mentioned before:

$$E_{\text{trap}} = E_{\text{g}} - (D_+ + D_-) + \frac{e^2}{4\pi\varepsilon R}.$$

When the incident beam is so weak that there is no saturation, the third term in Eq. (1) can be ignored because of the large distance between shallow trapped excitons. Therefore, E'_{trap} becomes

$$E'_{\text{trap}} = E_{\text{g}} - (D_+ + D_-). \tag{5}$$

As Eq. (5) is substituted for Eq. (1),

$$E_{\text{trap}} = E'_{\text{trap}} + \frac{e^2}{4\pi\varepsilon R}. \tag{6}$$

Therefore, the distance between two shallow trapped excitons are obtained as follows:

$$R = \frac{e^2}{4\pi\varepsilon(E_{\text{trap}} - E'_{\text{trap}})} = \frac{e^2}{4\pi\varepsilon \Delta E_{\text{trap}}}. \tag{7}$$

Here, the electronic charge is known and ΔE_{trap} is measured to be 10 nm from the blue shifted fluorescence. Thus, if the permittivity (ε) of Zintl phase LiSbTe$_2$ at the emission state is given, R can be obtained easily from Eq. (7). However, ε cannot be obtained directly from the electrical method or the refractive index measurement due to its powder type sample condition with the average diameter of 100 nm. Therefore, its value can only be estimated by the optical method with an absorption spectrum under low laser fluence and the fitting related to refractive index and dielectric function. For the estimation of ε, the electronic energy state of the excited state is assumed to be similar to that of the ground state. This makes it possible for the permittivity obtained by the excitation spectrum to be applied to the case of the blue shift of 390 nm band in the fluorescence spectrum.

The permittivity ε in any media is $K(\omega)\varepsilon_0$, where $K(\omega)$ is the dielectric function and ε_0 is the permittivity in vacuum. $K(\omega)$ is induced from the refractive index $n(\omega)$ and is also related to the absorption coefficient $\alpha(\omega)$, which is obtained from the absorption spectrum. $\alpha(\omega)$ in the solid is $A(\omega)/z$, where $A(\omega)$ is the absorbance and z is a beam pathlength, which can be obtained from the information on the average particle size, the density of LiSbTe$_2$, and the amount in unit volume. The filled circles in Fig. 6(a) show the transformation from $\alpha(\omega)$ to $n_i(\omega)$. $n_i(\omega)$ from the absorption spectra is to be fitted with the theoretically obtained refractive index using gas phase model for the shallow trapped excitons. The gas phase model regards charged oscillating particles interacting with external electromagnetic field as a harmonic oscillator without any interaction between them [28]. In our studies, it is
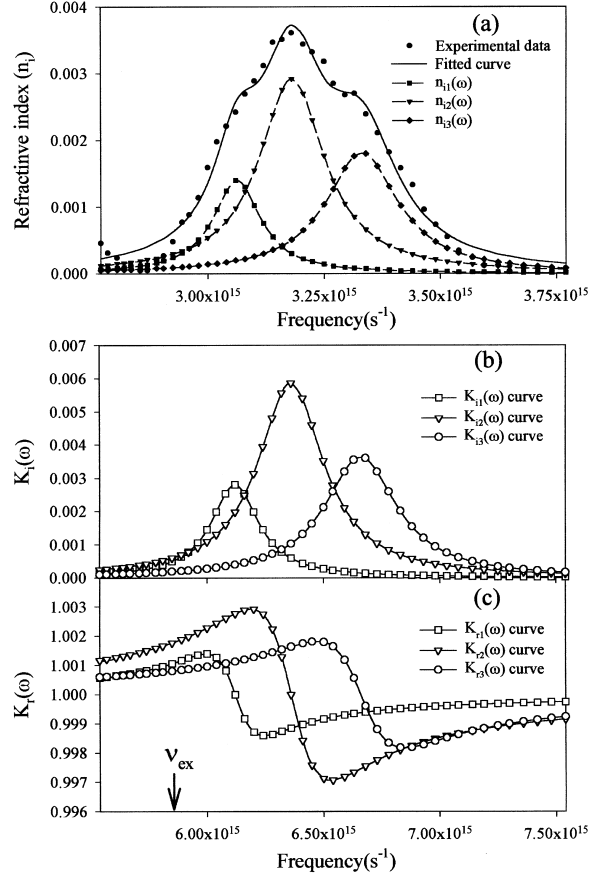

Fig. 6. (a) Imaginary part $n_i(\omega)$ of the refractive index of Zintl phase LiSbTe$_2$ at excitonic transition frequency; there are three Lorentzian type sub-bands. (b) Imaginary part of dielectric constant of Zintl phase LiSbTe$_2$ at excitonic transition frequency. (c) Real part of dielectric constant of Zintl phase LiSbTe$_2$ at excitonic transition frequency; the arrow mark indicates the excitation frequency.

considered that, at low excitation power, the density of exciton formed by the incident radiation is so small that the excitons in solid lattice can be treated as noninteracting gas molecules. Therefore, from the gas phase model, for a beam frequency ω close to the resonance frequency ω_0, $\omega^2 - \omega_0^2 \approx 2\omega_0(\omega - \omega_0)$, $n_i(\omega)$ is induced according to the procedure suggested in Ref. [28].

$$n_r(\omega) \approx 1 + \frac{\omega_p^2(\omega - \omega_0)/(4\omega_0\tau)}{(\omega - \omega_0)^2 + 1/(2\tau)^2}, \tag{8}$$

$$n_i(\omega) \approx \frac{\omega_p^2/(8\omega_0\tau)}{(\omega - \omega_0)^2 + 1/(2\tau)^2}, \tag{9}$$

where $n_r(\omega)$ is a real part of refractive index, $n_i(\omega)$ is an imaginary part of refractive index, τ is the damping time. Experimentally obtained $n_i(\omega)$ was fitted by three $n_i(\omega)$ with Eq. (9) as shown in Fig. 6(a). It is thought that the three $n_i(\omega)$ curves imply the vibrational energy states coupled to its electronically excited states at low temperature. Even though there is a possibility of more than three vibrational energy states in the excited states, the fitting using three $n_i(\omega)$ curves agreed well with the experimental data within our experimental error range. From the fitting with three $n_i(\omega)$ curves, we obtained the values of τ and ω_p^2 corresponding to each $n_i(\omega)$ and they were tabulated in Table 1.

With the gas phase model, three dielectric functions of the three vibrational energy states were obtained using the relationship between $n(\omega)$ and $K(\omega)$ given by the following equations [28]:

$$n_r(\omega) = 1 + \tfrac{1}{2}(K_r(\omega) - 1), \tag{10}$$

$$n_i(\omega) = \frac{K_i(\omega)}{2}, \tag{11}$$

where $K_r(\omega)$ is a real part of dielectric function and $K_i(\omega)$ is an imaginary part of dielectric function. Therefore $K_r(\omega)$ and $K_i(\omega)$ become

$$K_r(\omega) \approx 1 + \frac{\omega_p^2(\omega - \omega_0)/(2\omega_0\tau)}{(\omega - \omega_0)^2 + 1/(2\tau)^2}, \tag{12}$$

$$K_i(\omega) \approx \frac{\omega_p^2/(4\omega_0\tau)}{(\omega - \omega_0)^2 + 1/(2\tau)^2}. \tag{13}$$

With the values of τ and ω_p^2 that result from the $n_i(\omega)$ fitting, $K_r(\omega)$ and $K_i(\omega)$ were obtained according to the excitation frequencies as shown in

Table 1
Fitted parameters from the experimentally observed $n_i(\omega)$ with gas phase model

Parameter	$n_{i1}(\omega)$	$n_{i2}(\omega)$	$n_{i3}(\omega)$
ω_p^2 (s^{-2})	4.261×10^{28}	1.282×10^{28}	9.162×10^{28}
τ (s^{-1})	4.031×10^{-15}	2.910×10^{-15}	2.652×10^{-15}
K_r	1.001	1.002	1.001

Fig. 6(b) and (c). To estimate the separation distance between the shallow trapped excitons existing in the lattice at their saturation laser fluence, $K_r(\omega)\varepsilon_0$ of its excitation frequency was applied to ε in Eq. (7) due to the relatively very small value of $K_i(\omega)$. The calculated average distance at the excitation wavelength of 337 nm was about 17.6 nm. That is, the value 17.6 nm suggests the upper limit distance between two shallow trapped excitons at our laser fluence. The 390 nm band can be shifted further to the shorter wavelength as even higher laser fluence is applied to the sample, which suggests a distance shorter than 17.6 nm.

4. Conclusions

A newly synthesized ternary Zintl phase LiSbTe$_2$ is studied, for the first time, in order to investigate the fundamental electronic energy states by steady-state absorption, fluorescence, and fluorescence excitation spectroscopies. The results indicates that it has E_g of about 4.46 eV and there exists an absorption band around 300 nm below the band gap and the highly Stokes-shifted fluorescence band around 400 nm, which is often the case in chalcogenide compounds.

At liquid nitrogen temperature (77 K), the power dependent steady-state fluorescence studies revealed that other fluorescence bands appeared at about 450 and 520 nm. Both 390 and 520 nm emission bands were saturated at high laser fluence, and the 390 nm band shifted to the shorter wavelength by 10 nm at the laser fluence of the band saturation. From the power dependent time-resolved fluorescence studies at 77 K, it is known that 390, 450, and 520 nm emission bands had lifetimes of 3, 14, and 4 ns, respectively. The lifetime fitting of the fluorescence decay curves results in the amplitude changes of each lifetime component with an increase in the excitation power being in agreement with the results of the power dependent steady-state fluorescence spectra.

From the saturations and the comparisons of the fluorescence decay curves at 400 and 450 nm at both room and liquid nitrogen temperatures, it is suggested that the 390 nm band corresponds to the phonon coupled shallow trapped exciton states

with diffusive recombination governed by processes, such as exciton–phonon coupling, and the 450 nm band is from the deep-trapped localized exciton states induced by the lattice distortion, which seems to originate from the atomic size difference between Li and Sb and also the higher polarizing property of Li than that of Sb, and the broad 520 nm band occurs from the surface trap states interacting with the frozen solvent environment with a wide particle size distribution in our experimental limit.

The trial calculation for the separation distance between the trap sites was accomplished by applying the gas phase model to the excitons in the solid lattice. From the calculation, the upper limit distance between the shallow trapped exciton sites responsible for the 390 nm emission band is obtained to be about 17.6 nm.

Acknowledgements

References

[1] J.S. Jung, J. Zhang, C.J. O'Connor, in: S.M. Kauzlarich (Ed.), Chemistry, Structure, and Bonding of Zintl Phases and Ions, VCH publishers, New York, 1996, p. 275.

[2] R. Nesper, Angew. Chem. Int. Ed. Engl. 30 (1991) 789.

[3] V.A. Bazakutsa, N.I. Gnidash, V.B. Lazarev, E.I. Rogacheva, A.V. Salov, L.N. Sukhorukova, M.P. Vasil'eva, S.I. Berul', Russ. J. Inorg. Chem. 18 (1973) 1722.

[4] S.A. Tarasevich, I.S. Kovaleva, Z.S. Medvedeva, L.I. Antonova, Russ. J. Inorg. Chem. 16 (1971) 1522.

[5] I.S. Kovaleva, Z.S. Medvedeva, S.A. Tarasevich, L.I. Antonova, Russ. J. Inorg. Chem. 17 (1972) 1622.

[6] S.A. Tarasevich, Z.S. Medvedeva, I.S. Kovaleva, L.I. Antonova, J. Inorg. Chem. 17 (1972) 763.

[7] A. Ghosh, J. Phys.: Condens. Matter 1 (1989) 7819.

[8] V.P. Kochereshko, I.A. Merkulov, G.R. Pozina, I.N. Uraltsev, D.R. Yakovlev, W. Ossau, A. Waag, G. Landwehr, Solid-State Electron. 37 (1994) 1081.

[9] P. Bottcher, Angew. Chem. Int. Ed. Engl. 27 (1988) 759.

[10] R.C. Haushalter, L.J. Krause, Thin Solid Film 102 (1983) 161.

[11] R.C. Haushalter, Angew. Chem. 95 (1983) 560.

[12] R.C. Haushalter, C.J. O'Connor, A.M. Umarji, G.K. Shenoy, C.K. Saw, Solid-State Commun. 49 (1984) 929.

[13] J.S. Jung, L. Ren, C.J. O'Connor, J. Mater. Chem. 2 (1992) 829.

[14] B. Wu, L. Ren, C.J. O'Connor, J. Tang, J.S. Jung, J. Ferre, J.P. Jamet, J. Mater. Res. 9 (1994) 909.

[15] K. Binder, A.P. Young, Rev. Mod. Phys. 58 (1986) 801.

[16] M. Evain, F. Boucher, R. Brec, J. Rouxel, J.S. Jung, C.J. O'Conner, Eur. J. Solid-State Inorg. Chem. 29 (1992) 1055.

[17] L.M. Kovba, V.B. Lazarev, N.A. Moshchalkova, A.V. Salov, Russ. J. Inorg. Chem. 21 (1976) 257.

[18] C. Kittel, Introduction to Solid State Physics, sixth ed., Wiley, New York, 1986.

[19] F. Mauri, R. Car, Phys. Rev. Lett. 75 (1995) 3166.

[20] E. Hanamura, in: B.O. Seraphin (Ed.), Optical Properties of Solids, New Developments, North-Holland, Amsterdam, 1976 (Chapter 3).

[21] H.A. Klasens, J. Phys. Chem. Solids 7 (1958) 175.

[22] D.L. Rosen, Q.X. Li, R.R. Alfano, Phys. Rev. B 31 (1985) 2396.

[23] J. Warnock, D.D. Awschalom, Phys. Rev. B 31 (1985) 2360.

[24] K.C. Kao, W. Hwang, Electrical Transport in Solids, Pergamon Press, Oxford, 1981.

[25] S.I. Yang, Y.D. Suh, S.M. Jin, S.K. Kim, J.H. Park, E.J. Shin, D.H. Kim, J. Phys. Chem. 100 (1996) 9223.

[26] R.C. Powell, Z.G. Soos, Phys. Rev. B 5 (1972) 1547.

[27] N. Chestnoy, T.D. Harris, R. Hull, L.E. Brus, J. Phys. Chem. 90 (1986) 3393.

[28] M.V. Klein, Optics, Wiley, New York, 1976.